Electronic Supplementary Material (ESI) for Environmental Science: Nano.

Electronic Supporting Information

Nanoscale Control Over Water-Film Thickness Using Temperature Modulation: Tuning Mineral Carbonation Reactivity

Christopher J. Thompson[a]*, Sebastian T. Mergelsberg [b], Bavan P. Rajan[b], Paul F. Martin[a], Sebastien N. Kerisit[b], and John S. Loring[b]*

[a] Energy and Environment Directorate, Pacific Northwest National Laboratory, Richland, WA 99354, USA.

[b] Physical and Computational Sciences Directorate, Pacific Northwest National Laboratory, Richland, WA 99354, USA. E-mail: sebastian.mergelsberg@pnnl.gov and john.loring@pnnl.gov

*Corresponding Authors: chris.thompson@pnnl.gov and john.loring@pnnl.gov

This file contains 25 Pages, 11 Figures, and 3 Tables.

Table of Contents:

Materials and Methods

Materials. Nanosized forsterite (Mg_2SiO_4), with a nitrogen Brunauer-Emmet-Teller[1] (BET) determined specific surface area of 42.3 m^2/g, was used in this investigation. The synthesis and characteristics of the forsterite have previously been described in detail by Qafoku et al.[2] Carbon dioxide was purchased from Oxarc Inc. with a purity >99.999%. Reagent water was de-ionized (Barnstead NanoPure) and had a resistivity of 18.2 MΩ·cm.

Infrared Spectroscopic Titrations - General. *In situ* high-pressure IR titrations with H_2O were carried out at 50 °C and 90 bar in either supercritical CO_2 ($scCO_2$) or N_2 (scN_2) at using an automated fluid-delivery apparatus coupled to a custom-built high-pressure IR reaction cell (Figure S1A) with both transmission and attenuated total reflection (ATR) IR optics.[3, 4] IR spectra were collected using a Bruker Vertex 80V spectrometer equipped with a water-cooled source and a deuterated tri-glycine sulfate (DTGS) detector. The spectrometer was housed in an environmental chamber thermostated to 25 ± 0.2 °C. The high-pressure optical cell had an internal volume of 62.2 mL and is jacketed for temperature control by a circulating water bath. Temperature was monitored by a built-in, high-pressure, K-type thermocouple that is positioned within the main fluid cavity of the cell and was calibrated using ice and boiling water (see also IR Cell Temperature Measurements section below). Cell pressure was monitored by a pressure transducer that was calibrated against a NIST-traceable standard gauge. The transmission IR optics consisted of cylindrical ZnSe windows and a pathlength of ~4 cm. The internal reflection element (IRE) of the ATR IR optics was a single-reflection 45° prism made of Ge (Harrick Scientific). A detailed description of the fluid delivery apparatus, reaction cell, cell and manifold schematics, spectrometer settings, spectral collection procedures, titration loop calibrations, the general method for performing titrations, and data analysis procedures have been described in detail

elsewhere (see https://doi.org/10.1063/1.4870411).[3] Modifications to the transmission IR pathlength and the method for water delivery have also been described previously (https://doi.org/10.1021/acs.jced.6b00999).[4] In this study, the IRE was independently heated using two cartridge heaters installed in the mirror assembly beneath the IRE holder (Figure S1B). Voltage to the cartridge heaters was pulsed with a relay at a cycle time of 15 s and a dwell percentage that ranged from 0% (always off) to 100% (always on) using an EXTECH 48VFL proportional-integral-differential (PID) controller in manual mode.

IR Cell Temperature Measurements. Temperatures were measured at eight locations (see Table S1 and Figure S1C) on or within the high pressure IR cell for six dwell percentages applied to the cartridge heaters. The purpose of these measurements was to map the temperature differences within the cell so that condensation of diffused water vapor can be controlled during time-dependent IR titration experiments (see below) by changing the dwell percentage value. Location #1 was outside the fluid cavity at the base of the heated mirror assembly beneath the IRE holder. The other seven locations were within the main fluid cavity of the cell: (#2) above the IRE, (#3) above the cleanout plug, (#4) a transmission window of the cell, (#5) the sapphire window of the cell, (#6) the side of the cell cavity, halfway between the IRE and the sapphire window, (#7) the surface of the IRE, and (#8) where titrated liquid water pools. The temperature difference between where titrated liquid water pools (Location #7) the surface of the IRE (Location #8) is also listed in Table S1 for each dwell percentage. Measurements at the eight locations were made using T-type thermocouples that were calibrated against the built-in, high-pressure, K-type thermocouple (see above). Temperatures were measured using a 24-bit data acquisition board (USB-2416-4AO, Measurement Computing Corporation) that is interfaced to a computer through custom-written software. They are an average of 3600 measurements over a period of an hour and have a precision

of ±0.02 °C. The cell was under vacuum and thermostated at 50.00 ±0.03 °C according to the built-in high-pressure K-type thermocouple using the circulating water bath and cell water jacketing (see above). The circulating water bath programmatically holds at the temperature at 50.00°C by a feedback loop from the Type-K thermocouple, yet the temperatures at the other eight locations varied. The cell was allowed to equilibrate for at least 4 hours after a new dwell percentage was applied.

IR Spectroscopic Titrations – Time Dependent Experiments. Six titration experiments were performed to monitor forsterite carbonation in $scCO_2$ at 100% RH with excess liquid water present (TDep_CO2_1 through TDep_CO2_6; see Table S2). The purpose of these experiments was to estimate the amount of water adsorbed on the forsterite as a function of the temperature difference between the location where titrated liquid water pools (Location #7) and the surface of the IRE (Location #8), as well as to evaluate the dependence of forsterite carbonation on this amount of adsorbed water. Each experiment was carried out at one of the six dwell percentage values listed in Table S1. The dwell percentage was used to modulate the temperature difference between the surface of the IRE and the location where titrated liquid water pools. After a dwell percentage was applied, the cell was allowed to equilibrate under vacuum for at least 4 hours. Then, a background ATR IR spectrum was collected of the empty cell. Next, the cell was opened, and 0.1 mL of a 5 g/L forsterite suspension in isopropanol was evaporated under nitrogen gas flow onto the IRE to form an overlayer. The cell was then pressurized with anhydrous CO_2 to 90 bar at 50 °C. After collecting the background transmission IR spectrum of the anhydrous fluid and the ATR IR spectrum of the forsterite in contact with anhydrous $scCO_2$, twelve 1.9 μL additions of water were added to reach ~82% relative humidity (RH). After each addition, transmission IR and ATR IR spectra were acquired as a function of time for about 1 hr before the next addition was made. After

the twelfth addition of water, an additional ~10 μL of water was added to the cell at pressure to maintain the RH at 100% for the 5-day duration of the experiment. Based on the volume of cell and the concentration of dissolved H_2O at saturation in $scCO_2$ at 50 °C and 90 bar (see calibration experiments below), ~7 μL of this additional water remained in the liquid phase. The forsterite does not come in direct contact with this liquid water. Transmission IR and ATR IR spectra were acquired as a function of time (every 8 minutes) for 5 days. Time zero was defined as after the additional ~10 μL of water was added. Transmission IR spectra of the wet $scCO_2$ were processed in the HOH bending mode region of dissolved H_2O to determine RH. ATR IR spectra were of forsterite, and were collected to determine the amount of water adsorbed on forsterite and to follow the reactivity of forsterite towards carbonation. Details of the spectral processing are described below.

At the end of each experiment, the cell was dried by flushing with anhydrous CO_2 while maintaining temperature and pressure in order to quench the forsterite dissolution and carbonation reaction. Transmission IR spectra were collected during this drying procedure to monitor the RH. Once the RH was below 5%, the cell was depressurized slowly over a period of about 45 minutes. The sample was further dried by pulling a vacuum while flowing anhydrous CO_2 through it.

One additional titration experiment was carried out at a dwell percentage of 10.8% applied to the cartridge heaters, except using scN_2 instead of $scCO_2$ (TDep_N2_1; see Table S2). The purpose of this experiment was to estimate the amount of water adsorbed on forsterite at 100% RH with excess liquid water present, but under a condition where the forsterite is not dissolving and carbonating. For this experiment, three 1.9 μL additions of water were added to reach ~80% RH. After each addition, transmission IR and ATR IR spectra were acquired as a function of time for about 2 hr before the next addition was made. After the third addition of water, an additional ~8

μL of water was added to the cell at pressure to maintain the RH at 100% for the 5-day duration of the experiment. Based on the volume of cell and the concentration of dissolved H_2O at saturation in scN_2 at 50 °C and 90 bar (see calibration experiments below), ~7 μL of this additional water remained in the liquid phase.

IR Spectroscopic Titrations – Adsorbed Water Experiments. Five titration experiments (Ads_CO2_1 through Ads_CO2_5) were performed to determine the amount of water adsorbed on forsterite as a function of RH. The purpose of these experiments was also to calculate a correlation between the water coverage and the integrated absorbance of the OH stretch of adsorbed water. The IRE was not independently heated by cartridge heaters. For each experiment, a ~1.3g forsterite sample was prepared by evaporating an isopropanol suspension onto both sides of two relatively large glass slides (2.5 x 5.5 cm and 2.0 x 5.5 cm), vacuum drying at 50 °C overnight, and then re-equilibrating at ambient conditions before obtaining its mass. After a background ATR IR spectrum was collected of the empty cell, the two slides were inserted into the IR cell, and an additional 0.1 ml of a ~5 g/l forsterite suspension in isopropanol was pipetted onto IRE and dried with flowing nitrogen to form an ATR overlayer. The cell was then pressurized with anhydrous CO_2 to 90 bar at 50 °C. After collecting the background transmission IR spectrum of the anhydrous fluid and the ATR IR spectrum of the forsterite in contact with anhydrous $scCO_2$, fifteen 1.9 μL additions of water were added to reach ~82% RH. After each addition, transmission IR and ATR IR spectra were acquired as a function of time for ~1 hr before the next addition was made.

IR Spectroscopic Titrations – Calibrations. Several titration experiments were performed with the IR cell pressurized to 90 bar at 50 °C but in the absence of forsterite. The purpose of these experiments was to determine the correlation between concentration and absorbance of the HOH

bend of dissolved water, as well as to determine the concentration of water at saturation. Five titrations were carried out in $scCO_2$ (Cal_CO2_1 through Cal_CO2_5) using a 1.9 µL titration loop and ~1 hour between water additions, and three titrations were performed in scN_2 (Cal_N2_1 through Cal_N2_3) using a 0.78 µL titration loop and ~2 hours between water additions (Figure S2). The IRE was not independently heated by cartridge heaters in these experiments. A value of 24.6 ±0.1 mM was measured for the concentration of dissolved water at saturation in $scCO_2$, which is in good agreement with our previously reported 24.5±0.1 mM[4, 5] but higher than 23 mM predicted from the equation of state in Spycher et al.[6] A value of 6.0 ±0.2 mM was measured for the concentration of dissolved water at saturation in $scCO_2$, which is in good agreement with a value of 6.17 mM based on as study by Koglbauer and Wendland.[7, 8]

IR Spectral Processing. The following procedure was used to calculate RH values from transmission IR spectra. Spectra were first corrected to remove contributions from water vapor in the spectrometer and baseline drift by a classical-least squares fit to previously measured spectrum of water dissolved in the supercritical fluid ($scCO_2$ or scN_2) at 50 °C and 90 bar. The wavenumber regions used in the least-squares analysis were 813-1107, 1228-1567, 1650-2044, and 3821-4250 cm^{-1}. A linear baseline was also included in the fit for each wavenumber region. The residuals were almost exclusively the spectrum of water vapor, and the spectra were reconstructed using only the calculated contributions of water dissolved in the supercritical fluid. The integrated absorbance of the contribution from water dissolved in the supercritical fluid was calculated using the HOH bending mode region of dissolved water between 1650 and 2054 cm^{-1}. RH values were calculated by dividing the integrated absorbance measured after a water addition or at a specific reaction time by that absorbance when the supercritical fluid is fully saturated with water.

For adsorbed water experiments in $scCO_2$ (see above), transmission IR data were also used to calculate concentrations of water adsorbed to the forsterite as a function of RH (Figure S10). These values were calculated using the integrated absorbance of the HOH bend of dissolved water, as well as the correlation between the integrated absorbance and dissolved water concentration and the concentration of dissolved water in $scCO_2$ at saturation determined from IR cell calibration experiments (see Figure S2).

The following procedure was applied to ATR IR spectra to remove spectral contributions due to water vapor in the spectrometer, correct for baseline drift, and calculate integrated absorbances in the OH and CO stretching regions of water and carbonate. For the water vapor correction, a singular value decomposition was applied to an entire ATR experimental dataset in the region from 700 to 4200 cm^{-1}. Then the water vapor spectrum was subtracted from the first 11 eigenvectors (which account for 99.99998% of the variance in the data) using a spectrum of water vapor. Finally, each ATR IR spectrum was fit by classical least squares to the water vapor corrected eigenvectors and the spectrum of water vapor, but then reconstructed using only the calculated contributions of the 11 eigenvectors. For the baseline correction, ATR IR spectra were processed in the OH stretching region by subtracting the line fit to absorbances from 3877 to 3975 cm^{-1} and 2455 to 2502 cm^{-1}. Spectra were further baseline corrected in the asymmetric CO and SiO stretching regions by subtracting the average of the absorbances between 1892 and 1915 cm^{-1}. For the integrated absorbances, the water vapor and baseline corrected ATR IR spectra were first modified by subtracting the ATR IR spectrum of unreacted forsterite exposed to anhydrous supercritical fluid. In other words, the background ATR IR spectrum was changed from the empty cell under vacuum to the spectrum of unreacted forsterite under anhydrous fluid. Then, each

spectrum was integrated between 3050 and 3600 cm^{-1} for the OH stretching region and between 1400 and 1560 cm^{-1} for the CO stretching region.

Detailed Interpretation of the Spectra in Figures S3 through S8

Figures S3 through S6 (TDep_CO2_1 to TDep_CO2_4) are divided into three panels covering different reaction times of each experiment. Panel A shows spectra during the first 10 hrs of the experiments when the predominant changes are growth of OH stretching and HOH bending bands due to water adsorption and early growth of CO stretching bands of dissolved bicarbonate followed by hydromagnesite ($Mg_5(CO_3)_4(OH)_2 \cdot 4H_2O$). The spectra in panel B show continued increase in the CO stretching bands of hydromagnesite, increase in SiO stretching bands of amorphous silica, decrease in the CO stretching bands of bicarbonate, and decrease in SiO stretching bands of forsterite after 20 to 60 hours of reaction time. Select spectra for the remainder of the experimental reaction times (up to 5 days) are in panel C and show the decrease in the absorbance of OH stretching and HOH bending bands of adsorbed water, the growth of CO stretching bands of magnesite ($MgCO_3$), and the decrease in CO stretching bands of hydromagnesite.

Figures S7 and S8 (TDep_CO2_5 and TDep_CO2_6) are similarly divided into three panels, but bicarbonate was not detected, hydromagnesite was less predominant and magnesite nucleated earlier for TDep_CO2_5 (Figure S8), and magnesite was the only major carbonate observed in TDep_CO2_6 (Figure S8) and was preceded by what is likely amorphous magnesium carbonate (AMC; $MgCO_3 \cdot 0.5H_2O$) during the first 8 hours of the experiment. An additional time-dependent experiment (TDep_N2; see Table S2) was carried out at 100% RH in supercritical nitrogen (scN_2) when there was only a -0.01 °C temperature difference to compare to an experiment at the same temperature difference in reactive $scCO_2$. The spectra from this wet scN_2 experiment are not shown because only water adsorption was observed.

Table S1. Cell temperatures as a function of dwell percentage applied to the cartridge heaters used to independently heat the IRE of the high-pressure IR cell.[a]

	Location and Temperature (°C)								
Dwell Percentage (%)	#1 Mirror Assembly	#2 Above IRE	#3 Above Cleanout Plug	#4 Transmission Window	#5 Sapphire Window	#6 Side of Cavity	#7 Water Pool	#8 IRE Surface	Temp. Diff.[b] Between IRE Crystal Surface and Water Pool
0	47.83	50.03	49.83	50.41	49.96	50.56	50.33	50.04	-0.29
5.6	48.56	49.99	49.96	50.56	49.91	50.70	50.33	50.07	-0.26
8.0	49.31	50.01	49.86	50.48	49.90	50.61	50.43	50.27	-0.16
10.8	50.57	50.01	49.93	50.59	49.86	50.70	50.55	50.54	-0.01
13.8	52.15	50.01	49.78	50.49	49.80	50.58	50.69	50.45	0.16
18.8	54.77	49.95	49.70	50.48	49.65	50.53	50.89	51.40	0.51

[a] Cell was under vacuum when these measurements were made. Uncertainties in absolute temperatures are ±0.02°C. Uncertainty in temperature difference is ±0.03°C. See Figure S1 for a graphic showing locations.
[b] A negative temperature difference indicates that the IRE surface is cooler than the water pool.

Table S2. Time dependent experiments and their conditions.

Experiment	Supercritical Fluid	Dwell Percentage (%)	Temperature Difference Between IRE Crystal Surface and Water Pool Locations (°C) [a]
TDep_CO2_1	$scCO_2$	0	-0.29
TDep_CO2_2	$scCO_2$	5.6	-0.26
TDep_CO2_3	$scCO_2$	8.0	-0.16
TDep_CO2_4	$scCO_2$	10.8	-0.01
TDep_CO2_5	$scCO_2$	13.8	0.16
TDep_CO2_6	$scCO_2$	18.8	0.51
TDep_N2	scN_2	10.8	-0.01

[a] The water pool is Location #7, and the IRE Surface is Location #8; see Figure S1 and Table S1. A negative temperature difference indicates that the IRE surface (where the forsterite is located) is cooler than the water pool. Temperatures were measured when the IR cell was under vacuum. Uncertainty in temperature difference is ±0.03°C.

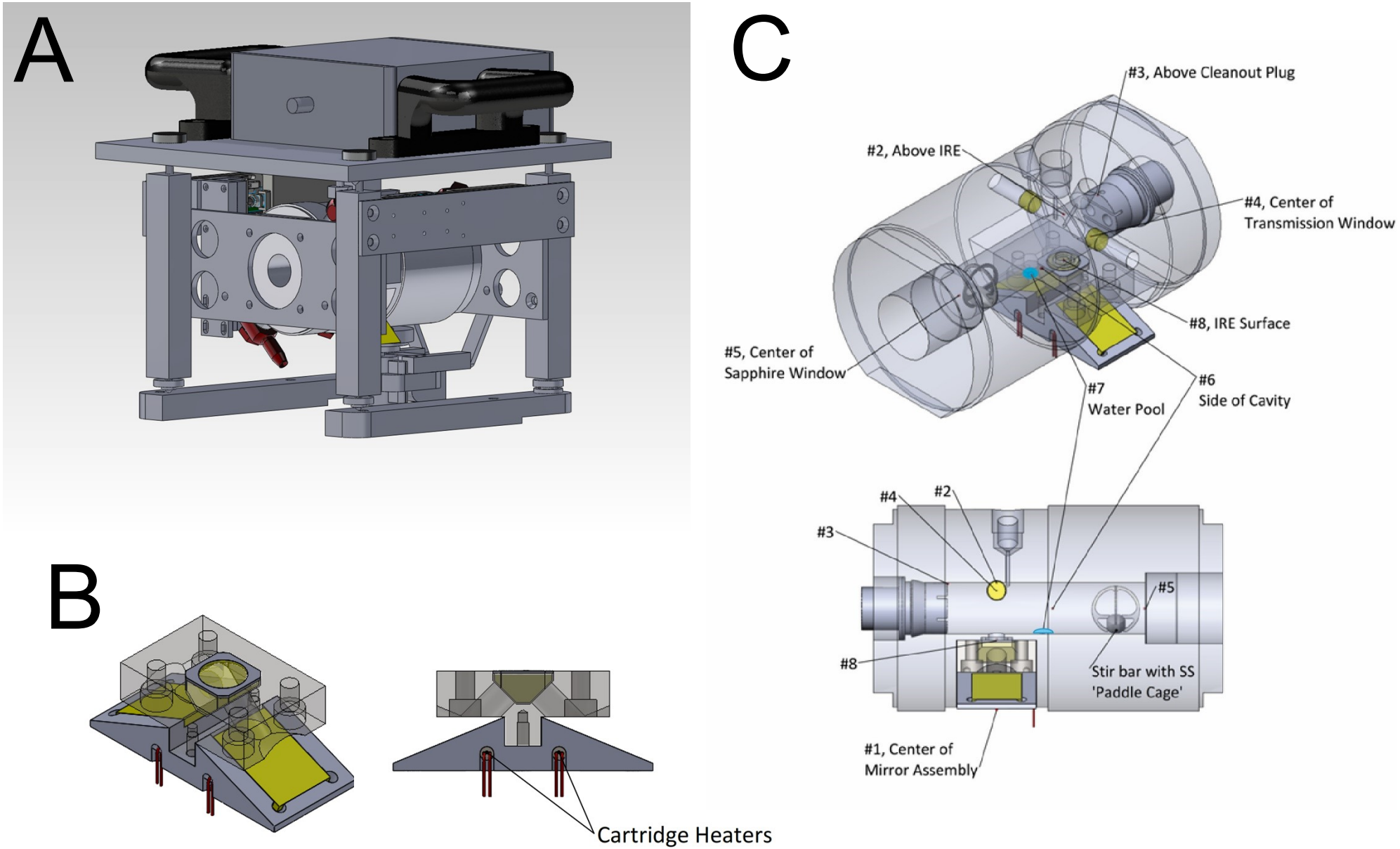

Figure S1. Schematics of the high-pressure IR titration cell. (A) Three-dimensional view of the assembled cell chassis. (B) Two views of the mirror assembly below the IRE holder with cartridge heaters. (C) The locations on or within the cell where temperatures were measured (see Table S1). See https://doi.org/10.1063/1.4870411 for more details about the cell design.

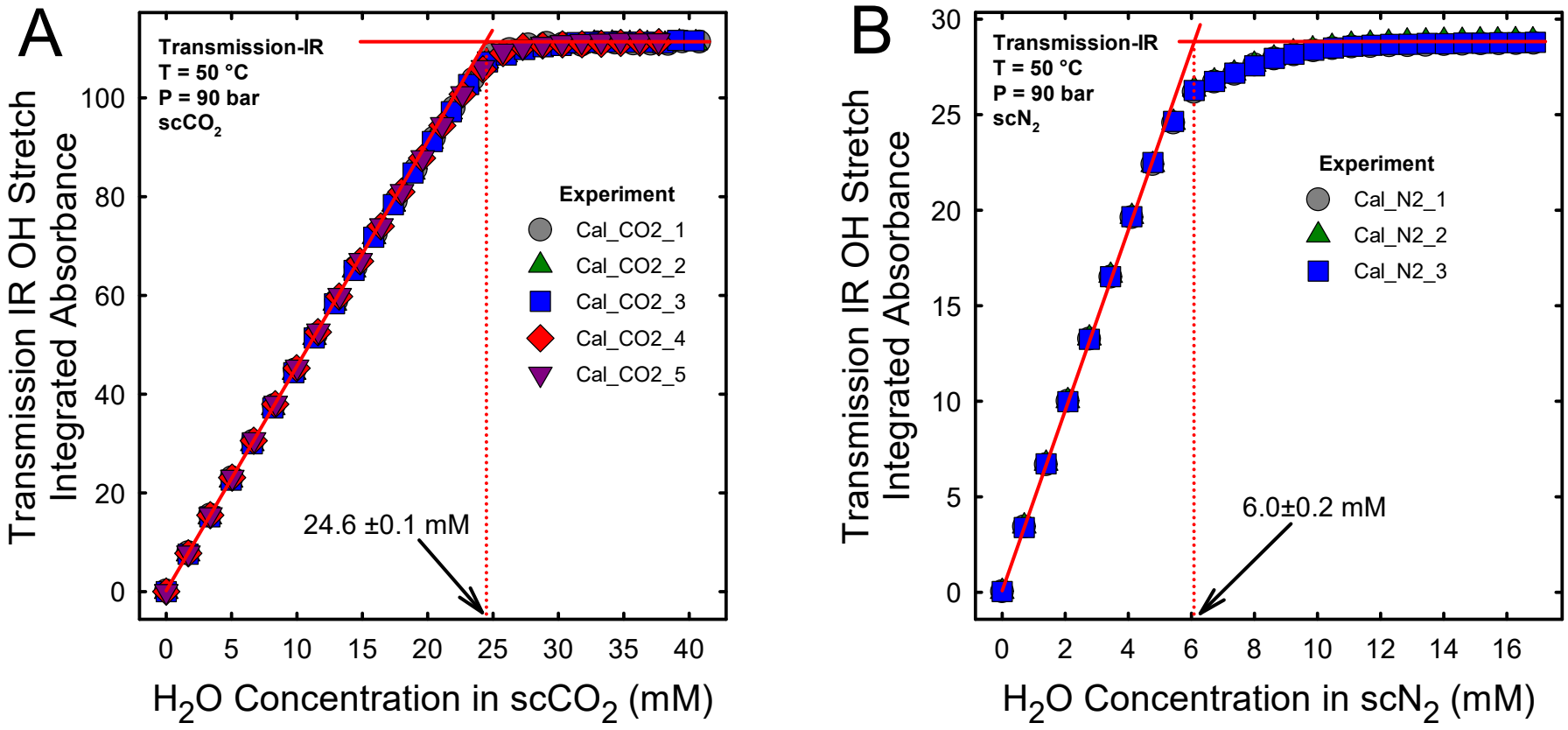

Figure S2. Transmission data from five IR titrations with H_2O at 50 °C and 90 bar of (A) $scCO_2$ and (B) scN_2. These plots show the integrated absorbance of the HOH bending mode of dissolved H_2O versus total H_2O concentration. The intersection of the straight lines fit through the linear and plateau regions of the data (overlapping symbols) is the dissolved H_2O concentration at saturation.

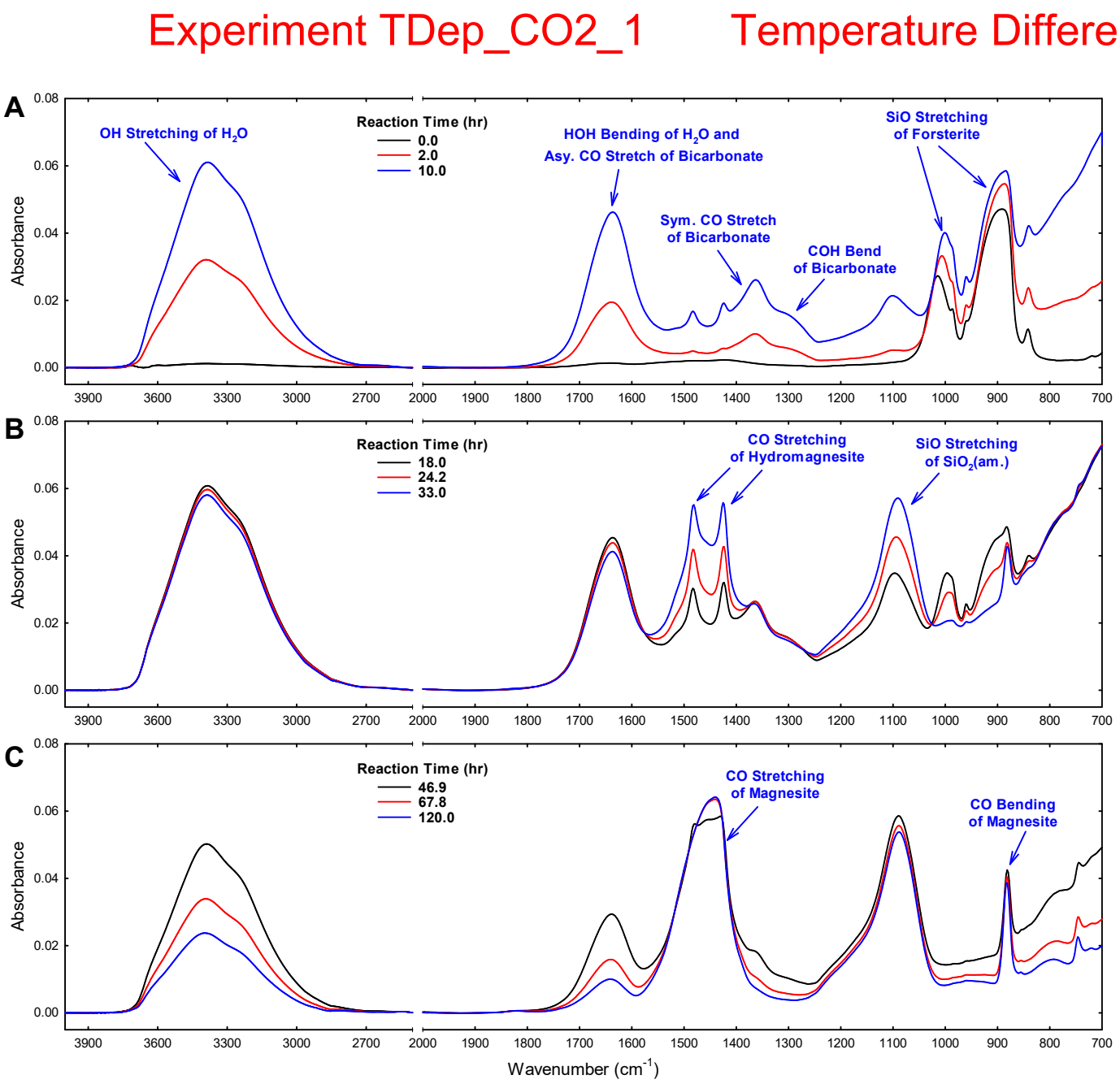

Figure S3. Selected in situ ATR IR spectra as a function of time from TDep_CO2_1 where forsterite was reacted in $scCO_2$ at 50 °C, 90 bar, and 100% RH with excess water present. The surface of the IRE where the forsterite was located (Location #8; see Table S1 and Figure S1) was 0.29 °C cooler than where the titrated liquid water pools (Location #7). The estimated average film thickness after 10 hour was 170 ML. These results demonstrate three reaction stages: (A) Water condenses onto the forsterite, as indicated by the growth of OH stretching and HOH bending modes. Forsterite dissolution by carbonic acid leads to Mg^{2+} and HCO_3^- dissolved in the water. (B) CO stretching bands tentatively assigned to hydromagnesite grow, as do SiO stretching bands of SiO_2(am). (C) The absence of SiO stretching bands of forsterite indicates that the parent mineral has been completely consumed. Growth of SiO stretching bands due to SiO_2(am) has ceased. Hydromagnesite transforms into more stable magnesite. The lower solubility of magnesite leads to decrease of bands due to bicarbonate. Adsorbed water decreased, possibly due to lower concentrations of Mg^{2+} and HCO_3^- or redistribution of water to locations in the IR cell that are cooler than the IRE surface.

Experiment TDep_CO2_2 Temperature Difference = -0.26 °C

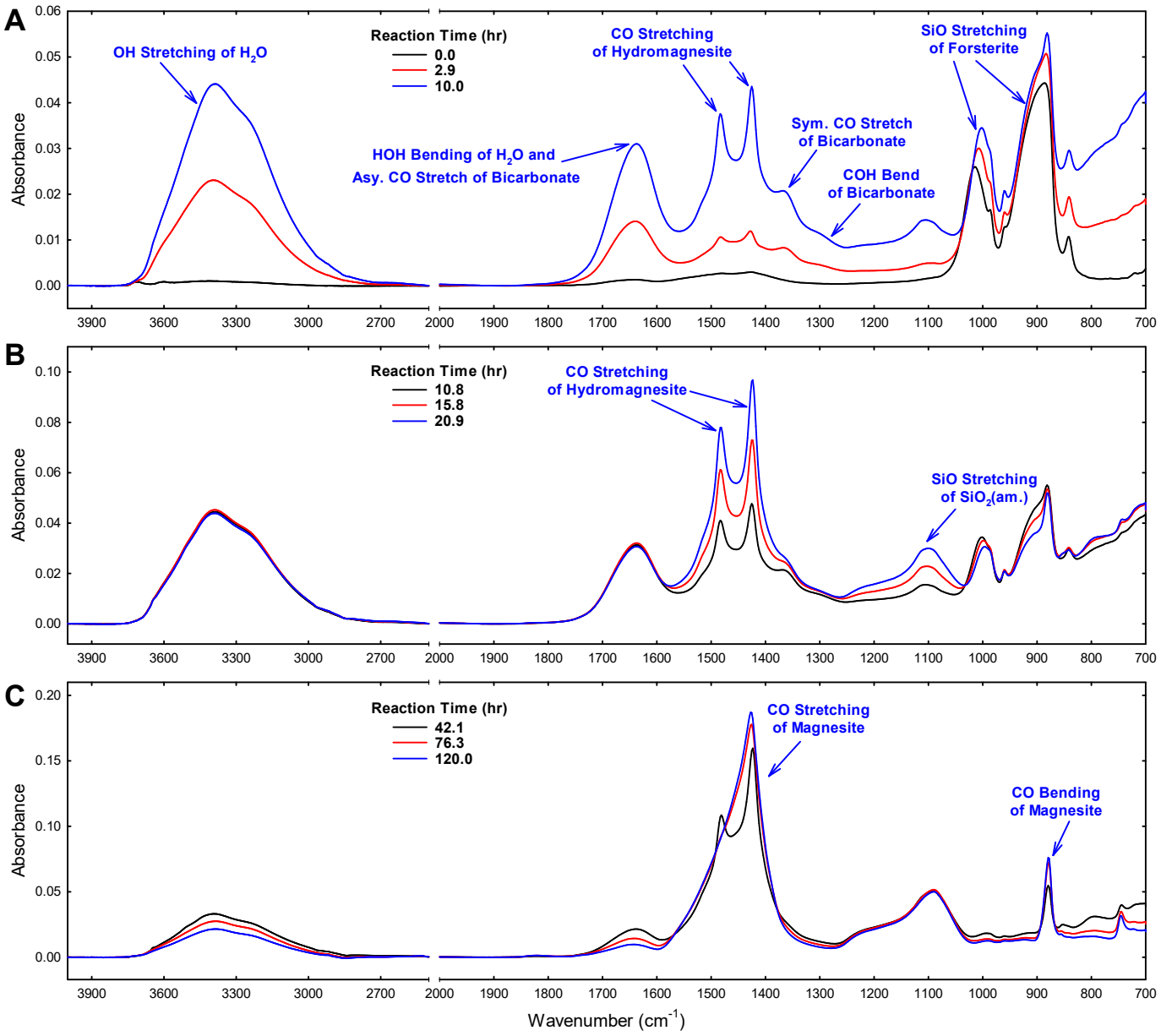

Figure S4. Selected in situ ATR IR spectra as a function of time from TDep_CO2_2 where forsterite was reacted in $scCO_2$ at 50 °C, 90 bar, and 100% RH with excess water present. The surface of the IRE where the forsterite was located (Location #8; see Table S1 and Figure S1) was 0.26 °C cooler than where the titrated liquid water pools (Location #7). The estimated average film thickness after 10 hour was 120 ML. These results are similar to those for experiment TDep_CO2_1 and demonstrate three reaction stages: (A) Water condenses onto the forsterite, as indicated by the growth of OH stretching and HOH bending modes. Forsterite dissolution by carbonic acid leads to Mg^{2+} and HCO_3^- dissolved in the water. CO stretching bands tentatively assigned to hydromagnesite grow in absorbance. (B) CO stretching bands of hydromagnesite continue to grow, as do SiO stretching bands of SiO_2(am). (C) The absence of SiO stretching bands of forsterite indicates that the parent mineral has been completely consumed. Growth of SiO stretching bands due to SiO_2(am) has ceased. Hydromagnesite transforms into more stable magnesite. The lower solubility of magnesite leads to decrease of bands due to bicarbonate. Adsorbed water decreased, possibly due to lower concentrations of Mg^{2+} and HCO_3^- or redistribution of water to locations in the IR cell that are cooler than the IRE surface.

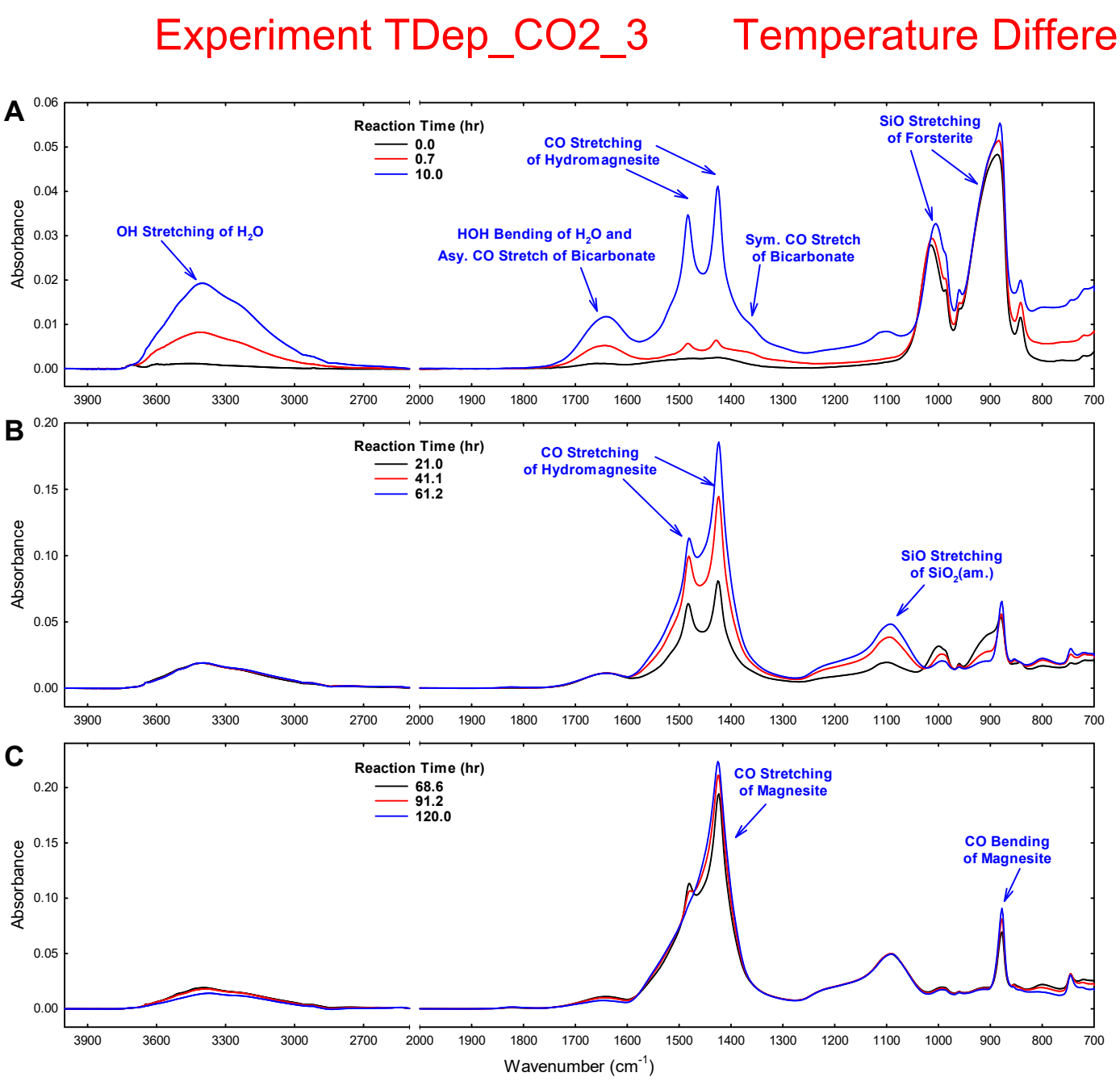

Figure S5. Selected in situ ATR IR spectra as a function of time from TDep_CO2_3 where forsterite was reacted in $scCO_2$ at 50 °C, 90 bar, and 100% RH with excess water present. The surface of the IRE where the forsterite was located (Location #8; see Table S1 and Figure S1) was 0.16 °C cooler than where the titrated liquid water pools (Location #7). The estimated average film thickness after 10 hour was 53 ML. These results demonstrate three reaction stages: (A) Water condenses onto the forsterite, as indicated by the growth of OH stretching and HOH bending modes. Forsterite dissolution by carbonic acid leads to Mg^{2+} and HCO_3^- dissolved in the water. CO stretching bands tentatively assigned to hydromagnesite grow, as do SiO stretching bands of SiO_2(am). (B) Hydromagnesite grows until magnesite nucleates. Hydromagnesite begins to transform to magnesite. SiO stretching bands of SiO_2(am) continue to grow. (C) The absence of SiO stretching bands of forsterite indicates that the parent mineral has been completely consumed. Growth of SiO stretching bands due to SiO_2(am) has ceased. Hydromagnesite has nearly completely transformed into more stable magnesite. Adsorbed water decreased, possibly due to lower concentrations of Mg^{2+} and HCO_3^- or redistribution of water to locations in the IR cell that are cooler than the IRE surface.

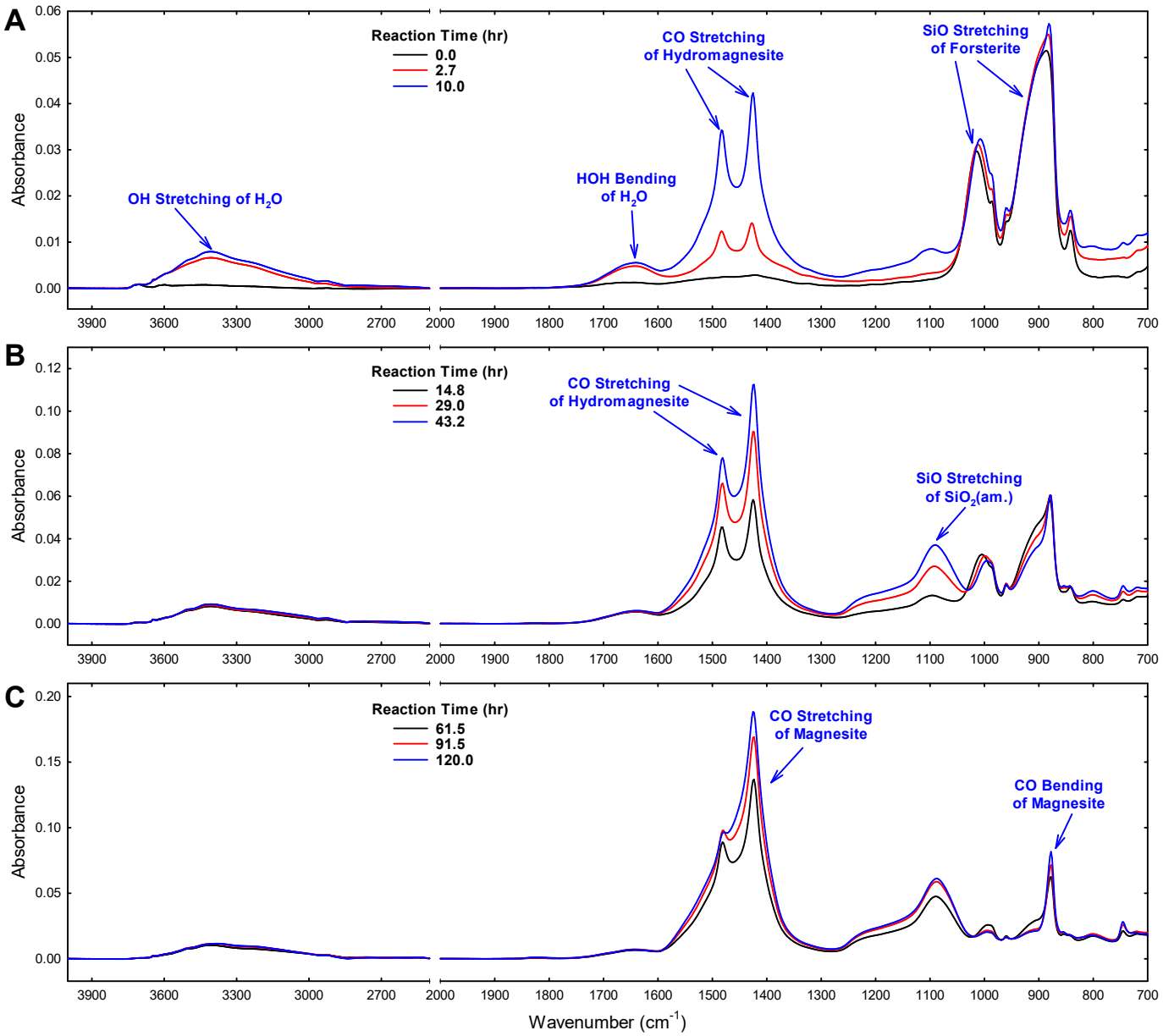

Figure S6. Selected in situ ATR IR spectra as a function of time from TDep_CO2_4 where forsterite was reacted in $scCO_2$ at 50 °C, 90 bar, and 100% RH with excess water present. The surface of the IRE where the forsterite was located (Location #8; see Table S1 and Figure S1) was 0.01 °C cooler than where the titrated liquid water pools (Location #7). The estimated average film thickness after 10 hour was 21 ML. These results are similar to those for experiment TDep_CO2_3 and demonstrate three reaction stages: (A) Water condenses onto the forsterite, as indicated by the growth of OH stretching and HOH bending modes. Forsterite dissolution by carbonic acid leads to Mg^{2+} and HCO_3^- dissolved in the water. CO stretching bands tentatively assigned to hydromagnesite grow, as do SiO stretching bands of SiO_2(am). (B) Hydromagnesite grows until magnesite nucleates. Hydromagnesite begins to transform to magnesite. SiO stretching bands of SiO_2(am) continue to grow. (C) The SiO stretching bands of forsterite have diminished and the growth of SiO stretching bands due to SiO_2(am) has slowed. Hydromagnesite has nearly completely transformed into more stable magnesite.

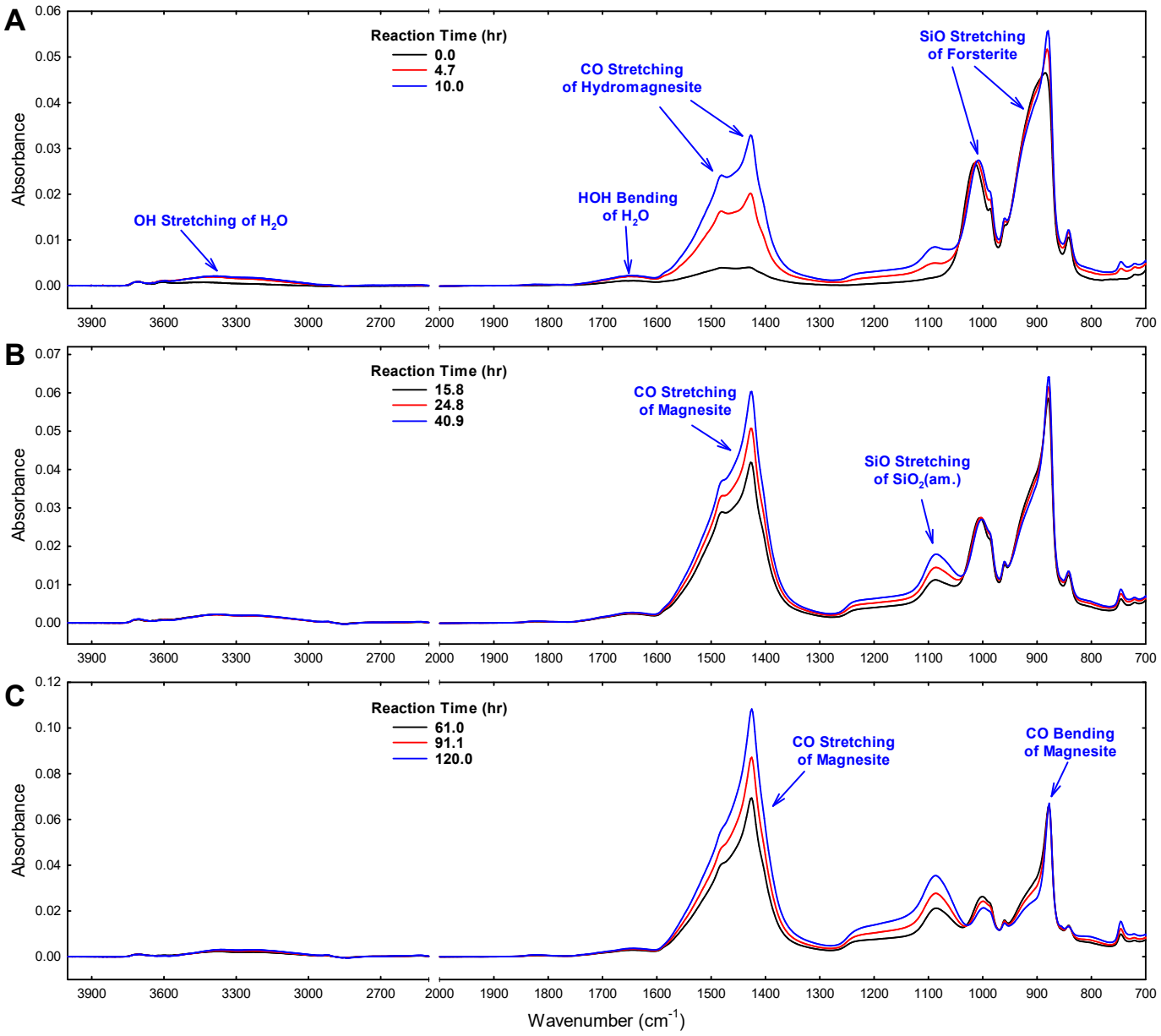

Figure S7. Selected in situ ATR IR spectra as a function of time from TDep_CO2_5 where forsterite was reacted in $scCO_2$ at 50 °C, 90 bar, and 100% RH with excess water present. The surface of the IRE where the forsterite was located (Location #8; see Table S1 and Figure S1) was 0.16 °C warmer than where the titrated liquid water pools (Location #7). The estimated average film thickness after 10 hour was 5.8 ML. These results demonstrate three reaction stages: (A) Water condenses onto the forsterite, as indicated by the growth of OH stretching and HOH bending modes. CO stretching bands tentatively assigned to hydromagnesite grow early in the experiment, but magnesite soon nucleates. Magnesite grows, and hydromagnesite transforms to magnesite. SiO stretching bands of SiO_2(am) grow. (B) Magnesite continues to grow while hydromagnesite is consumed. SiO stretching bands of SiO_2(am) continue to grow. (C) The SiO stretching bands of forsterite diminish while those bands due to SiO_2(am) grow. Magnesite continues to grow. Hydromagnesite has nearly completely transformed into more stable magnesite.

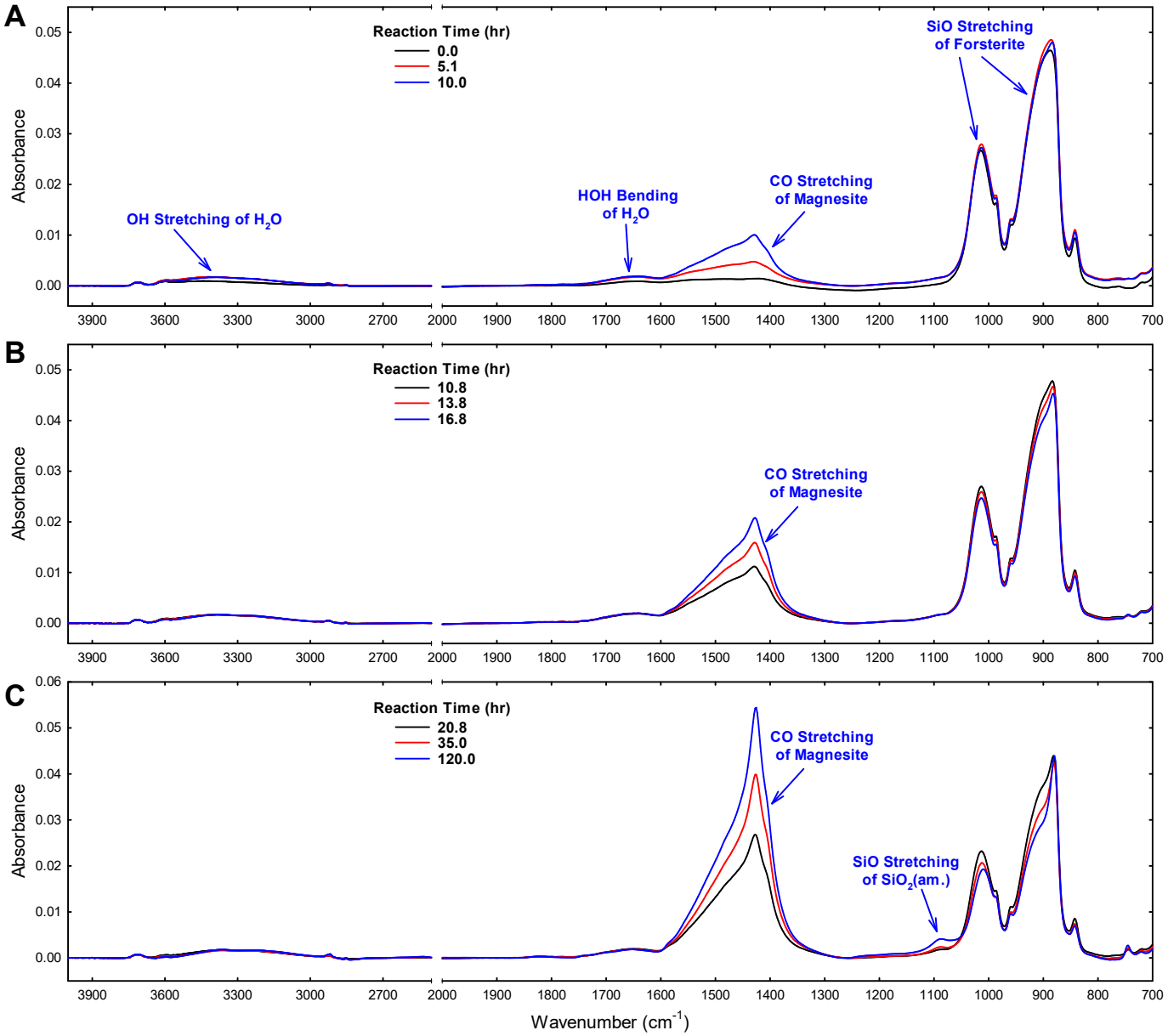

Figure S8. Selected in situ ATR IR spectra as a function of time from TDep_CO2_6 where forsterite was reacted in $scCO_2$ at 50 °C, 90 bar, and 100% RH with excess water present. The surface of the IRE where the forsterite was located (Location #8; see Table S1 and Figure S1) was 0.51 °C warmer than where the titrated liquid water pools (Location #7). The estimated average film thickness after 10 hour was 4.7 ML. The results demonstrate three reaction stages: (A) Water condenses onto the forsterite, as indicated by the growth of OH stretching and HOH bending modes. Magnesite nucleates and grows. There is little evidence of hydromagnesite except possibly at the earliest reaction time. (B) Magnesite continues to grow. The SiO stretching bands of forsterite decrease. (C)) Magnesite continues to grow. The SiO stretching bands of forsterite continue to decrease. Growth of SiO stretching bands due to SiO_2(am) become apparent.

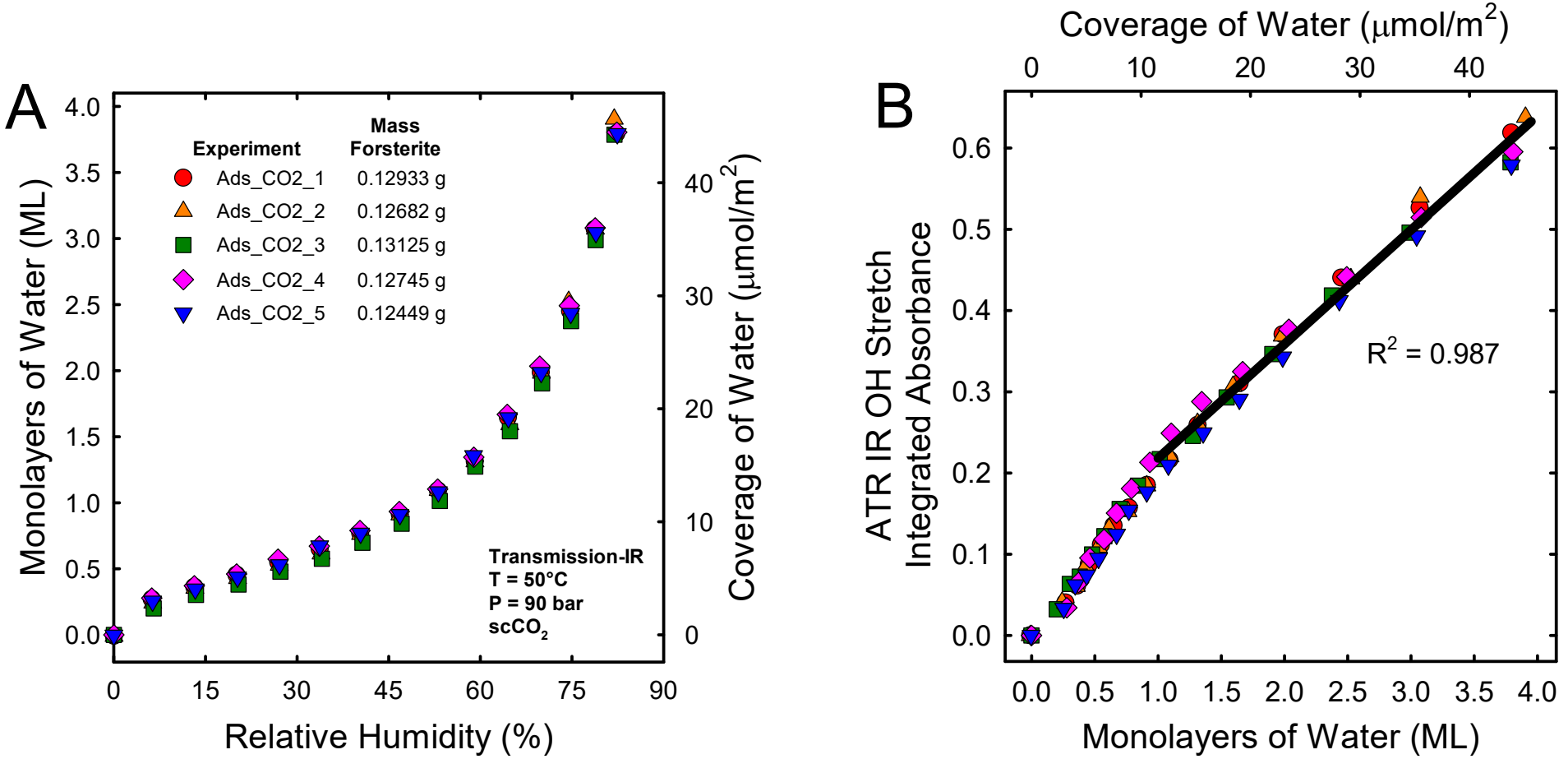

Figure S9. (A) Average water film thickness in units of both monolayers (ML) and μmol/m^2 as a function of relative humidity (RH) for experiments Ads_CO2_1 through Ads_CO2_5 where forsterite was titrated with water in $scCO_2$ at 90 bar and 50 °C. The uncertainty in the water film thickness is estimated to be ± 0.05 ML based on the reproducibility of the IR titration experiments. (B) The integrated absorbance in the OH stretching region (specifically, between 3050 and 3600 cm^{-1}) as a function of water film thickness. The black line is the linear least squares fit to the data beyond 1 monolayer of water. This correlation was used to estimate the average water film thickness in experiments TDep_CO2_1 through TDep_CO2_6 (see Figure 1 in the main text). See also Figure S11 and the main text for more details.

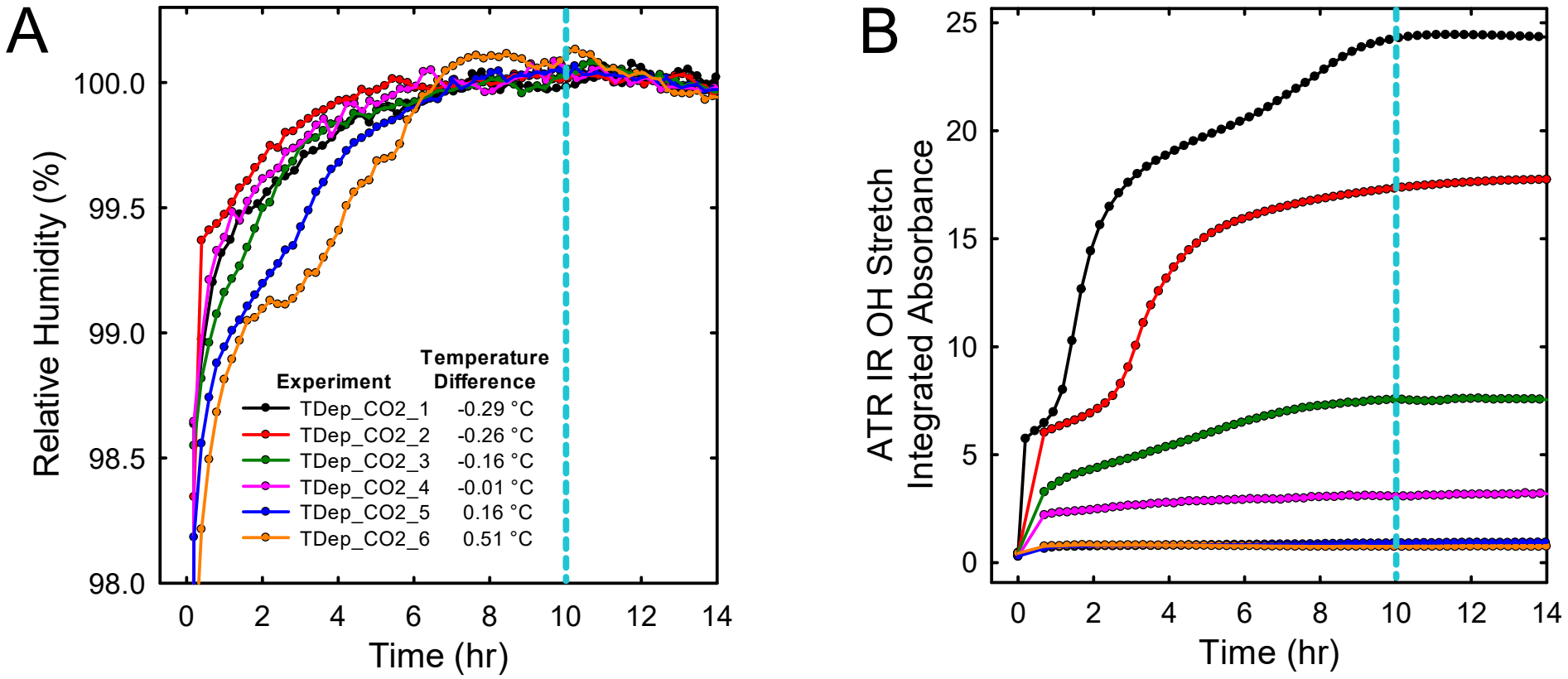

Figure S10. (A) Relative humidity (RH) as a function of time from experiments TDep_CO2_1 through TDep_CO2_6 (see Table S2) where forsterite was reacted for a total of 120 hours in $scCO_2$ at 50 °C, 90 bar, and 100% RH with excess water present. In this study, 10 hours (blue dashed vertical line) was considered the time required for the liquid water titrated into the cell at time zero to dissolve to an extent so that the fluid was fully saturated (100% RH). (B) The integrated absorbance in the OH stretching region (specifically, between 3050 and 3600 cm^{-1}) from ATR IR spectra collected as a function of time during experiments TDep_CO2_1 through TDep_CO2_6. The blue dashed vertical line at 10 hours indicates the integrated absorbance when the $scCO_2$ had reached 100% RH. This integrated absorbance was used to estimate the average water film thickness in these experiments (see Figure 1 in the main text) according to the linear least squares correlation in Figure S10B. The legend in (A) is also for (B). The lines between the data points are to help visualize trends.

Details of Water Film Thickness Analysis Using κ-Köhler Theory

During the carbonation of forsterite, CO_2 dissolves into the water film to form carbonic acid, which reacts with the mineral to form the magnesium carbonate and amorphous silica. The resulting magnesium carbonate is initially quite soluble, as initial precipitates are primarily amorphous magnesium carbonate (AMC). Thus, we assume that the formation of water layers is most likely due to dissolution of forsterite into the water layer and net water uptake due to the hygroscopic effect. There are many different ways to model this effect.[9] Here, we use a modified hygroscopic growth model adapted from Irwin et al. and others[10-14] to relate the hydrated particle diameter at temperature T (D_T) to the water vapor saturation, S:

$$S = \frac{\left(\frac{D_T}{D_0}\right)^3 - 1}{\left(\frac{D_T}{D_0}\right)^3 - (1-\kappa)} e^{\left(\frac{4\gamma V_m}{RTD_T}\right)} \quad \text{(S1)}$$

Where D_0 is the dry particle diameter ($D_0 = 2r = 26.2$ nm) and κ is an empirical hygroscopicity parameter.[9] D_T is calculated as D_0 plus the thickness of a water monolayer times the number of monolayers, using the same convention as experiment.

To calculate the vapor saturation, S, we first estimate the concentration of water dissolved in the $scCO_2$, c, from the equations of state by Spycher.[6] Actual concentrations derived this way are summarized in Table S3. To turn these values into estimates of water saturation near the sample, we make the following 3 assumptions: 1) The temperature gradient above the sample is

very steep, 2) the bulk $scCO_2$ phase is in equilibrium with the water pool at 50 °C, and 3) The degree of water saturation near the sample can thus be defined as follows:

$$S = \frac{c}{c_{sat}} = \frac{c_{50\,°C}}{c_{T_{sample}}} \quad \text{(S2)}$$

Where $c_{T_{sample}}$ is the concentration at the temperature of the sample and $c_{50\,°C}$ is the concentration near the water concentration in equilibrium with the water pool.

Using these estimates of S from equation S2, we then fit κ in Equation S1 to relate hygroscopicity to water film thickness and reactivity. The values produced by the model are generally within the range of values expected from literature and reproduces the experimental values well. Predicted hygroscopicity values for thicker water films at the lower temperatures are consistent with values measured for other silicate minerals, close to $\kappa = 0.1$.[9] This likely corresponds to a surface that is dominated by magnesium carbonate phases. Thinner films, on the other hand, are approximately one order of magnitude less hygroscopic, likely because they may have large amounts of exposed amorphous silica near the surface. This fit to the data (Figure S11) is meant to qualitatively illustrate the applicability of a hygroscopy model to the measured data and does not reflect a rigorous quantitative analysis. For this, measurements of V_m, γ, and κ as functions of monolayer thickness on forsterite would be necessary.

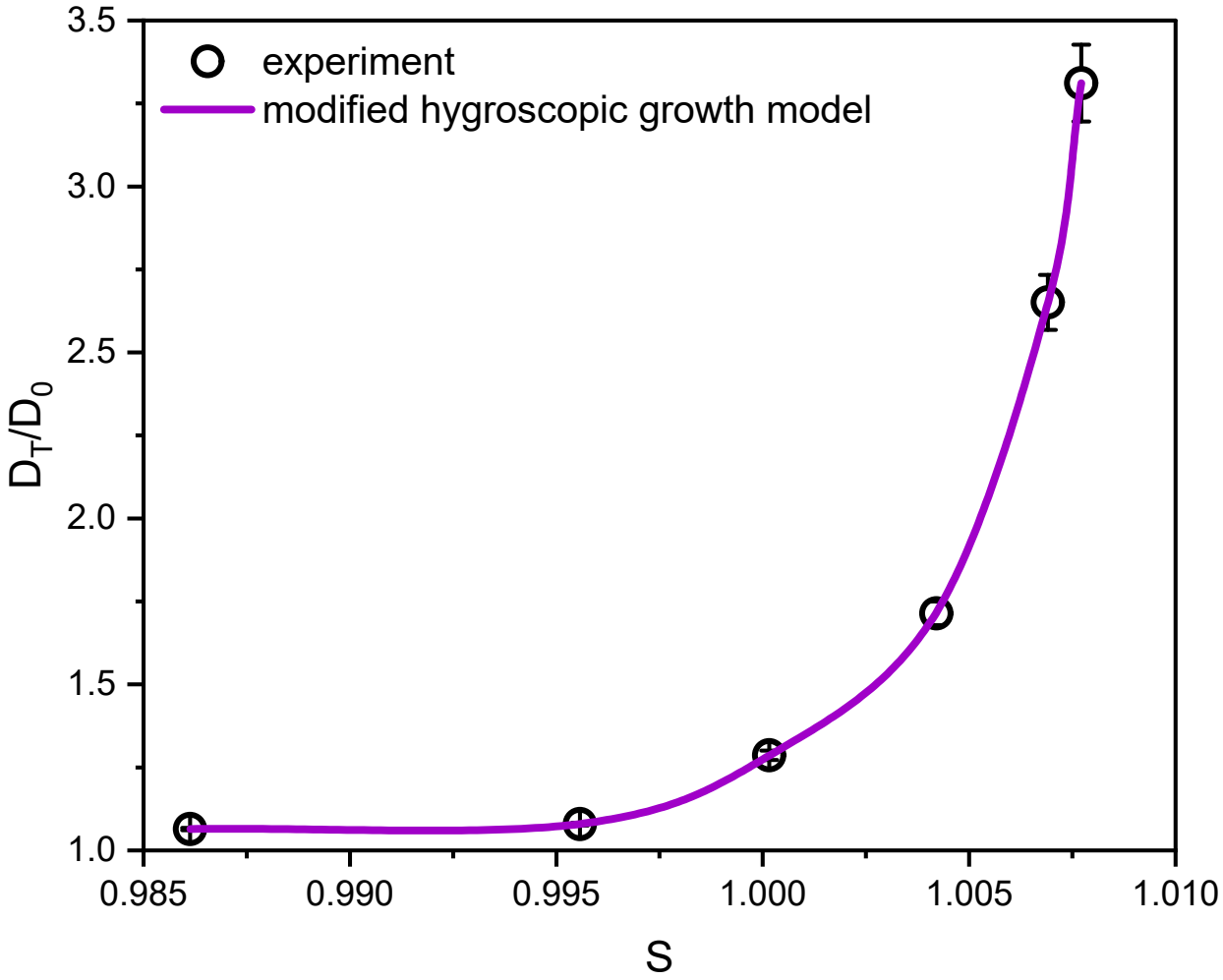

Figure S11. Fit of modified hygroscopic growth model to data. Summary of values given in Table S3.

Table S3. Summary of measured and calculated values used in the analysis above.

Temperature °C	ΔT °C	c_{H2O} ppmw	ML_{H2O}	S_{exp}	ML_{exp}	D_T/D_0	κ	S_{calc}
49.71	-0.29	1438.8	170.3	1.0077	170.3	3.31	0.10568	1.0077
49.74	-0.26	1439.9	121.6	1.0069	121.6	2.65	0.11410	1.0069
49.84	-0.16	1443.8	52.6	1.0042	52.6	1.71	0.06682	1.0042
49.99	-0.01	1449.6	21.1	1.0002	21.1	1.29	0.03127	1.0002
50.00	0.00	1449.7	--	--	--	--	--	--
50.16	0.16	1456.2	5.8	0.9956	5.8	1.08	0.00973	0.9956
50.51	0.51	1469.7	4.7	0.9861	4.7	1.06	0.00993	0.9861

SI References

1. S. Brunauer, P. H. Emmett and E. Teller, *Journal of the American Chemical Society*, 1938, **60**, 309-319.
2. O. Qafoku, E. S. Ilton, M. E. Bowden, L. Kovarik, X. Zhang, R. K. Kukkadapu, M. H. Engelhard, C. J. Thompson, H. T. Schaef, B. P. McGrail, K. M. Rosso and J. S. Loring, *Journal of Colloid and Interface Science*, 2018, **515**, 129-138.
3. C. J. Thompson, P. F. Martin, J. Chen, P. Benezeth, H. T. Schaef, K. M. Rosso, A. R. Felmy and J. S. Loring, *Rev Sci Instrum*, 2014, **85**.
4. J. S. Loring, D. H. Bacon, R. D. Springer, A. Anderko, S. Gopinath, C. M. Yonkofski, C. J. Thompson, B. P. McGrail, K. M. Rosso and H. T. Schaef, *Journal of Chemical & Engineering Data*, 2017, **62**, 1608-1614.
5. Q. R. S. Miller, E. S. Ilton, O. Qafoku, D. A. Dixon, M. Vasiliu, C. J. Thompson, H. T. Schaef, K. M. Rosso and J. S. Loring, *J Phys Chem Lett*, 2018, DOI: 10.1021/acs.jpclett.8b02162, 4988-4994.
6. N. Spycher, K. Pruess and J. Ennis-King, *Geochimica et Cosmochimica Acta*, 2003, **67**, 3015-3031.
7. G. Koglbauer and M. Wendland, *Journal of Chemical & Engineering Data*, 2008, **53**, 77-82.
8. P. J. Linstrom and W. G. Mallard, *Journal of Chemical & Engineering Data*, 2001, **46**, 1059-1063.
9. M. Tang, D. J. Cziczo and V. H. Grassian, *Chemical Reviews*, 2016, **116**, 4205-4259.
10. M. Irwin, N. Good, J. Crosier, T. W. Choularton and G. McFiggans, *Atmos. Chem. Phys.*, 2010, **10**, 11737-11752.
11. H. Herich, T. Tritscher, A. Wiacek, M. Gysel, E. Weingartner, U. Lohmann, U. Baltensperger and D. J. Cziczo, *Physical Chemistry Chemical Physics*, 2009, **11**, 7804-7809.
12. M. Gysel, E. Weingartner and U. Baltensperger, *Environmental Science & Technology*, 2002, **36**, 63-68.
13. B. Svenningsson, J. Rissler, E. Swietlicki, M. Mircea, M. Bilde, M. C. Facchini, S. Decesari, S. Fuzzi, J. Zhou, J. Mønster and T. Rosenørn, *Atmos. Chem. Phys.*, 2006, **6**, 1937-1952.
14. M. D. Petters and S. M. Kreidenweis, *Atmos. Chem. Phys.*, 2007, **7**, 1961-1971.